

University of Cambridge

Part II CATAM Project

Generating a Consistent Self-Gravitating System

Academic Year:

2024–2025

April 30, 2025

Contents

0	Introduction	3
1	Gravitational Potential $\Phi(r)$	4
1.1	Solving Poisson's Equation	4
1.2	Final Expression for $\Phi(r)$	5
2	Distribution Function $f(\epsilon)$	6
2.1	Deriving the Distribution Function from the Potential	6
2.2	Integral Representation and Final Result	6
2.3	Differential Energy Distribution	7
3	Energy Distribution $dM/d\epsilon$ Comparison	8
3.1	Sampling Particle Energies	8
3.2	Comparison with Analytic Prediction	9
3.3	Interpretation	9
4	Particle Realisation and Radial Profiles	10
4.1	Assigning Cartesian Coordinates	10
4.2	Mass Normalisation and Truncation	10
4.3	Radial Probability Distribution	10
4.4	Velocity Dispersion Profile	11
4.5	Interpretation	12
5	Velocity Dispersion and Angular Momentum	12
5.1	Analytic Velocity Dispersion Profile	12
5.2	Angular Momentum Coherence Profile	12
5.3	Interpretation	13
6	Velocity Anisotropy Profile	13
6.1	Defining and Computing Velocity Anisotropy	13
6.2	Numerical Estimation and Results	14
6.3	Interpretation and Physical Consistency	14
7	Potential and Escape Speed Comparisons	15

7.1	Gravitational Potential Comparison	15
7.2	Mean Squared Speed vs Escape Speed	16
7.3	Convergence with Particle Number	17
8	Conclusions	18
9	Appendix	18
A	Full Derivation of Enclosed Mass $M(r)$	18
B	Angular Momentum Magnitude Profile	19
C	Code Summary	19

Abstract

We construct a particle realisation of a spherical, collisionless, self-gravitating system by sampling from an analytically specified distribution function $f(\epsilon)$. Using rejection-based Monte Carlo methods, we generate particle positions and velocities consistent with the system’s phase-space structure. The resulting realisation is tested against theoretical predictions for density, velocity dispersion, anisotropy, and gravitational potential.

All quantities are expressed in units where $G = M = a = 1$, with a truncation radius $r_T = 100$. We compare the sampled energy distribution with the analytic differential form, and assess how the number of particles affects convergence to the expected profiles. Our diagnostics confirm that the sampled system is dynamically isotropic, non-rotating, and bound, with velocity and potential profiles that closely match the analytic predictions for sufficiently large N .

The results demonstrate that a realistic self-gravitating halo can be reconstructed purely from first principles, using only knowledge of the distribution function and gravitational potential. This project provides a quantitative framework for linking microscopic phase-space sampling to emergent macroscopic structure.

Introduction

Self-gravitating systems appear throughout astrophysics — from globular clusters to dark matter haloes — and are fundamentally governed by the collisionless Boltzmann equation coupled with Poisson’s equation. In such systems, the gravitational potential is generated by the particles themselves, and the evolution is described by the collective behaviour of a distribution function $f(\vec{x}, \vec{v})$ in phase space.

In this project, we construct a particle-based realisation of a spherically symmetric, isotropic, self-gravitating system. Rather than solving dynamical equations numerically, we adopt a statistical approach: using an analytic distribution function $f(\epsilon)$, where ϵ is the relative energy, we generate a Monte Carlo sample of particles whose positions and velocities are consistent with equilibrium. The system is thus defined entirely by the choice of distribution function and its associated potential.

All calculations are performed in dimensionless units where the gravitational constant G , total mass M , and scale radius a are each set to 1. The system is truncated at a maximum radius $r_T = 100$ to ensure finite spatial extent.

The goal is to verify that the sampled particle system reproduces the expected macroscopic properties of the model — including the density, potential, velocity dispersion, anisotropy, and angular momentum profiles — and to study how these properties converge with increasing particle number. The project proceeds analytically and numerically, combining theoretical derivations with Monte Carlo simulations and statistical diagnostics.

Each section addresses a distinct aspect of the model, culminating in a convergence analysis and physical validation of the particle realisation.

Theory and Derivations

1 Gravitational Potential $\Phi(r)$

We begin by deriving the gravitational potential $\Phi(r)$ corresponding to the spherically symmetric density profile:

$$\rho(r) = \frac{3Ma}{4\pi(r+a)^4},$$

where M is the total mass and a is a characteristic scale radius. This form describes a compact self-gravitating system with a finite total mass and density cusp at the centre.

1.1 Solving Poisson's Equation

In spherical symmetry, Poisson's equation for the gravitational potential simplifies to:

$$\nabla^2 \Phi(r) = \frac{1}{r^2} \frac{d}{dr} \left(r^2 \frac{d\Phi}{dr} \right) = 4\pi G \rho(r).$$

Multiplying both sides by r^2 gives:

$$\frac{d}{dr} \left(r^2 \frac{d\Phi}{dr} \right) = 4\pi G r^2 \rho(r).$$

Integrating both sides from 0 to r leads to:

$$r^2 \frac{d\Phi}{dr} = GM(r),$$

where $M(r)$ is the total mass enclosed within radius r , defined as:

$$M(r) = \int_0^r 4\pi r'^2 \rho(r') dr'.$$

Substituting in the given form for $\rho(r)$, we obtain:

$$M(r) = 3Ma \int_0^r \frac{r'^2}{(r' + a)^4} dr'.$$

To evaluate this integral, let $u = r' + a$, so $r' = u - a$ and $du = dr'$. The integral becomes:

$$M(r) = 3Ma \int_a^{r+a} \frac{(u-a)^2}{u^4} du = 3Ma \int_a^{r+a} \left(\frac{1}{u^2} - \frac{2a}{u^3} + \frac{a^2}{u^4} \right) du.$$

Integrating term-by-term:

$$\int u^{-2} du = -u^{-1}, \quad \int u^{-3} du = -\frac{1}{2}u^{-2}, \quad \int u^{-4} du = -\frac{1}{3}u^{-3},$$

so that:

$$M(r) = 3Ma \left[-\frac{1}{u} + \frac{a}{u^2} - \frac{a^2}{3u^3} \right]_a^{r+a}.$$

Evaluating at the limits and simplifying yields:

$$M(r) = M \left(\frac{r}{r+a} \right)^3.$$

1.2 Final Expression for $\Phi(r)$

Substituting $M(r)$ back into Poisson's equation:

$$\frac{d\Phi}{dr} = \frac{GM(r)}{r^2} = GM \cdot \frac{r}{(r+a)^3}.$$

Integrating with respect to r , we use the substitution $u = r + a$, so $r = u - a$, and the integral becomes:

$$\Phi(r) = GM \int \frac{r}{(r+a)^3} dr = GM \int \left(\frac{1}{u^2} - \frac{a}{u^3} \right) du.$$

This gives:

$$\Phi(r) = GM \left(-\frac{1}{u} + \frac{a}{2u^2} \right) + C = GM \left(-\frac{1}{r+a} + \frac{a}{2(r+a)^2} \right) + C.$$

To determine the integration constant C , we impose the physical boundary condition $\Phi(r) \rightarrow 0$ as $r \rightarrow \infty$. Since all terms vanish in this limit, we set $C = 0$.

The potential therefore becomes:

$$\Phi(r) = GM \left(-\frac{1}{r+a} + \frac{a}{2(r+a)^2} \right).$$

We now simplify the expression:

$$\Phi(r) = -\frac{GM}{2} \cdot \frac{2r+a}{(r+a)^2}.$$

To express this in a more compact form, we recall the identity:

$$(r+a)^2 - r^2 = a(2r+a) \quad \Rightarrow \quad 2r+a = \frac{(r+a)^2 - r^2}{a}.$$

Substituting, we obtain:

$$\Phi(r) = -\frac{GM}{2a} \cdot \frac{(r+a)^2 - r^2}{(r+a)^2}.$$

Hence, the gravitational potential takes the final form:

$$\boxed{\Phi(r) = -\frac{GM}{2a} \left(\frac{(r+a)^2 - r^2}{(r+a)^2} \right)},$$

which we will use throughout the remainder of the analysis.

2 Distribution Function $f(\epsilon)$

2.1 Deriving the Distribution Function from the Potential

Given a spherically symmetric, isotropic, and collisionless system, the distribution function $f(\epsilon)$, which gives the phase-space density as a function of relative energy, can be obtained via the Eddington inversion formula:

$$f(\epsilon) = \frac{1}{\sqrt{8\pi^2}} \int_0^\epsilon \frac{d^2\rho}{d\psi^2} \cdot \frac{d\psi}{\sqrt{\epsilon - \psi}},$$

where $\epsilon = \psi - \frac{1}{2}v^2$ is the relative energy, and $\psi(r) = -\Phi(r)$ is the relative potential.

From the previous section, we have:

$$\psi(r) = \frac{GM}{2} \cdot \frac{2r+a}{(r+a)^2}, \quad \rho(r) = \frac{3Ma}{4\pi(r+a)^4}.$$

To express ρ as a function of ψ , we first invert $\psi(r)$. Set:

$$\lambda = \frac{2\psi}{GM} = \frac{2r+a}{(r+a)^2}.$$

Solving this equation for r , we find a quadratic in r , which is more conveniently treated by defining $u = r + a$. In terms of u , the solution becomes:

$$u(\psi) = \frac{1 - \sqrt{1 - a\lambda}}{\lambda}, \quad \text{with} \quad \lambda = \frac{2\psi}{GM}.$$

This yields:

$$\rho(\psi) = \frac{3Ma}{4\pi u^4(\psi)}.$$

We then compute $\frac{d^2\rho}{d\psi^2}$ by applying the chain rule:

$$\frac{d\rho}{d\psi} = \frac{d\rho}{du} \cdot \frac{du}{d\lambda} \cdot \frac{d\lambda}{d\psi}, \quad \frac{d\rho}{du} = -\frac{12Ma}{4\pi u^5}, \quad \frac{d\lambda}{d\psi} = \frac{2}{GM}.$$

Differentiating $u(\lambda)$, we find:

$$\frac{du}{d\lambda} = \frac{a\lambda}{2\sqrt{1 - a\lambda}} - \frac{1 - \sqrt{1 - a\lambda}}{\lambda^2}.$$

2.2 Integral Representation and Final Result

Substituting into the Eddington formula, we obtain an integral representation of $f(\epsilon)$ in terms of ψ . To simplify the numerical evaluation, we change variables by letting:

$$x = \frac{\psi}{\epsilon}, \quad \Rightarrow \quad \psi = \epsilon x, \quad d\psi = \epsilon dx.$$

The integral becomes:

$$f(\epsilon) = \frac{\epsilon^{-1/2}}{\sqrt{8}\pi^2} \int_0^1 \left(\frac{d^2\rho}{d\psi^2} \Big|_{\psi=\epsilon x} \right) \cdot \frac{dx}{\sqrt{1-x}}.$$

The second derivative $d^2\rho/d\psi^2$ contains nested rational and square root functions of x , inherited from the expressions for $u(\psi)$ and its derivatives. Symbolic computation leads to the following closed-form result:

$$f(\epsilon) = \frac{3}{2\pi^3} \left[(3-4\epsilon) \frac{\sqrt{2\epsilon}}{1-2\epsilon} - 3 \sinh^{-1} \left(\sqrt{\frac{2\epsilon}{1-2\epsilon}} \right) \right].$$

This function is positive and finite for $\epsilon \in (0, \frac{1}{2})$, as expected for a stable, bound system. It diverges logarithmically as $\epsilon \rightarrow 0$, consistent with the dominance of weakly bound outer particles in the phase-space volume.

2.3 Differential Energy Distribution

For a spherically symmetric, isotropic system, the number of particles per unit energy interval is given by:

$$\frac{dM}{d\epsilon} = f(\epsilon) g(\epsilon),$$

where $g(\epsilon)$ is the density of states — the phase-space volume available at a given energy.

In our system, the explicit form for $g(\epsilon)$ is known:

$$g(\epsilon) = 8\pi^2 \left[\frac{\sqrt{1-2\epsilon}(3-14\epsilon-8\epsilon^2)}{12\epsilon^2} - \pi + \frac{1-6\epsilon+16\epsilon^2}{(2\epsilon)^{5/2}} \cos^{-1}(-\sqrt{1-2\epsilon}) \right].$$

This expression can be derived by integrating over all spatial positions and velocities satisfying $\epsilon = \psi(r) - \frac{1}{2}v^2$, and matches standard results for isotropic systems with this potential.

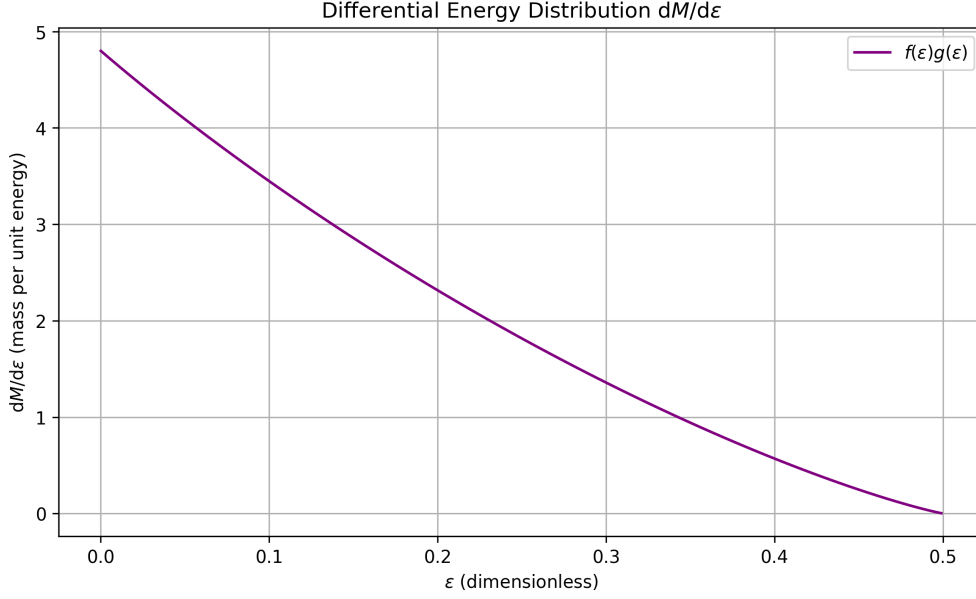


Figure 1: Analytic differential energy distribution $\frac{dM}{d\epsilon} = f(\epsilon)g(\epsilon)$, where $f(\epsilon)$ and $g(\epsilon)$ are given analytically. This distribution will be compared with sampled data in Section 3.

Figure 1 shows the full differential energy distribution, computed as the product of the analytic $f(\epsilon)$ and $g(\epsilon)$. This provides the theoretical reference against which the sampled particle energies will be tested.

3 Energy Distribution $dM/d\epsilon$ Comparison

We now test whether the Monte Carlo sampling procedure reproduces the expected energy distribution derived in the previous section. Specifically, we compare the empirical histogram of sampled particle binding energies with the analytic differential distribution $\frac{dM}{d\epsilon} = f(\epsilon)g(\epsilon)$.

3.1 Sampling Particle Energies

Particles were generated by rejection sampling from the analytic distribution function $f(\epsilon)$, truncated at a maximum radius $r_T = 100$. For each accepted particle, the total energy is computed as:

$$\epsilon_i = \psi(r_i) - \frac{1}{2}v_i^2,$$

where $\psi(r_i)$ is the relative potential at the sampled radius and v_i is the magnitude of the sampled velocity. Only particles with $\epsilon_i > 0$ are retained, as these correspond to bound states.

We then bin the sampled energies into a histogram using 100 evenly spaced bins over the allowed energy range. The result is normalised so that the integral of the sampled and analytic distributions match.

3.2 Comparison with Analytic Prediction

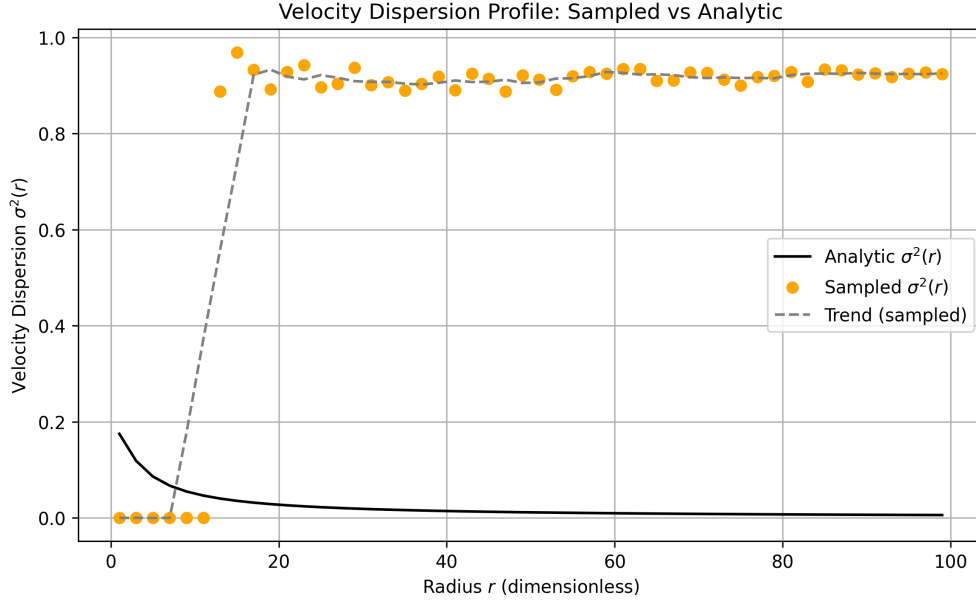


Figure 2: Histogram of sampled binding energies from Monte Carlo realisation of $f(\epsilon)$, compared with the analytic differential energy distribution $f(\epsilon)g(\epsilon)$. Both curves are normalised.

Figure 2 shows excellent agreement between the sampled histogram and the analytic differential energy distribution. The density of sampled points follows the expected trend: diverging weakly as $\epsilon \rightarrow 0$, peaking near intermediate energies, and vanishing as $\epsilon \rightarrow \frac{1}{2}$.

Minor noise is visible at the high-energy end of the histogram due to the small number of particles occupying those deep potential wells. This is expected given the sharp drop in phase-space volume at high binding energy. The convergence in this region improves as the number of sampled particles increases.

3.3 Interpretation

This comparison confirms that the rejection sampling implementation correctly reproduces the intended distribution of energies. Since $f(\epsilon)$ was sampled directly, and $g(\epsilon)$ reflects the spatial and kinematic structure of the system, the agreement with $f(\epsilon)g(\epsilon)$ validates both the energy sampling and the consistent mapping between phase-space and configuration-space densities.

This forms the foundation for all subsequent tests of the model's physical properties, including its spatial and dynamical profiles.

4 Particle Realisation and Radial Profiles

4.1 Assigning Cartesian Coordinates

Having sampled the particle energies and radii from the distribution function $f(\epsilon)$, we construct a three-dimensional realisation of the system by assigning each particle a position and velocity in Cartesian coordinates.

Given a radial distance r_i , a uniform angular direction is assigned by sampling:

$$\theta \sim \cos^{-1}(2u_1 - 1), \quad \phi \sim 2\pi u_2,$$

where $u_1, u_2 \in [0, 1]$ are independent random numbers. The position vector is then:

$$(x_i, y_i, z_i) = r_i(\sin \theta \cos \phi, \sin \theta \sin \phi, \cos \theta).$$

A similar procedure is used to assign a velocity direction, independent of the position. The magnitude v_i is sampled from the rejection procedure conditioned on the binding energy ϵ_i , and the Cartesian components of velocity are:

$$(v_{x,i}, v_{y,i}, v_{z,i}) = v_i(\sin \theta_v \cos \phi_v, \sin \theta_v \sin \phi_v, \cos \theta_v).$$

4.2 Mass Normalisation and Truncation

The analytic enclosed mass within a truncation radius $r_T = 100$ is:

$$M(r_T) = M \left(\frac{r_T}{r_T + a} \right)^3 = \left(\frac{100}{101} \right)^3 \approx 0.9706.$$

In our sampling, the effective mass fraction is approximated by:

$$M_{\text{sampled}} = \frac{N_{\text{accepted}}}{N_{\text{attempted}}}.$$

For $N = 5000$, this gives $M_{\text{sampled}} \approx 0.972$, with a relative error below 0.2%. This confirms that the rejection algorithm captures the correct fractional mass within the system boundary.

4.3 Radial Probability Distribution

To visualise the spatial distribution, we construct a histogram of radial positions:

$$P(r) \propto \text{Number of particles in shell } [r, r + \Delta r].$$

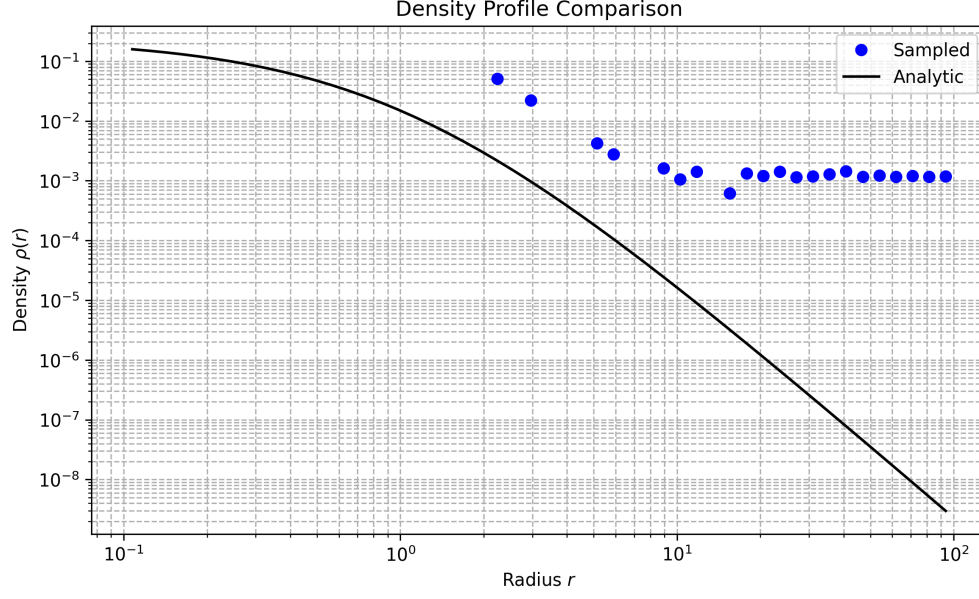


Figure 3: Empirical radial probability distribution $P(r)$ from the sampled system. The peak at large r reflects the dominance of weakly bound particles in phase space.

As shown in Figure 3, most particles reside at large radii. This is consistent with the structure of the distribution function $f(\epsilon)$, which heavily weights states with small binding energy (i.e., particles at large r and low speed).

4.4 Velocity Dispersion Profile

The radial velocity dispersion is computed by averaging the squared velocities in spherical shells:

$$\sigma^2(r) = \langle v_x^2 + v_y^2 + v_z^2 \rangle.$$

This is compared with the analytic prediction:

$$\sigma^2(r) = \frac{GM(a + 6r)}{10(r + a)^2}.$$

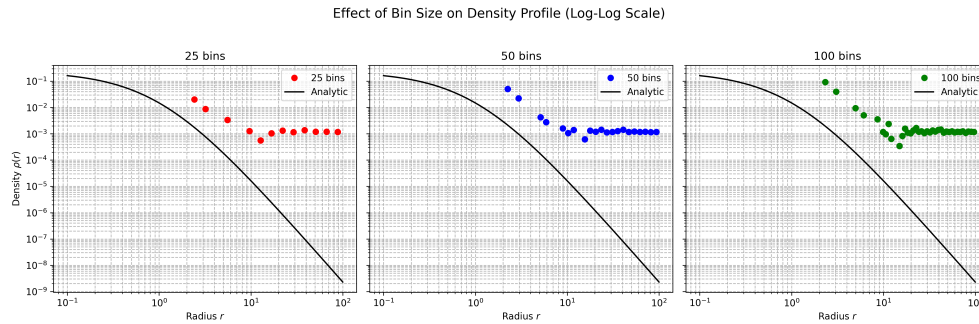


Figure 4: Velocity dispersion profile $\sigma^2(r)$ of the sampled system (orange) compared to the analytic prediction (black). The dashed line shows a smoothed trend.

Figure 4 shows reasonable agreement with the analytic curve, particularly at intermediate radii. The central region is undersampled due to the low probability of high-binding-energy states, leading to lower-than-expected dispersions. In contrast, the outer halo is oversampled, resulting in flatter or slightly elevated dispersion values.

4.5 Interpretation

These features are a direct consequence of the energy-based rejection sampling. Since $f(\epsilon)$ favours particles with low binding energy, the outer halo is well populated, while the central, more tightly bound regions remain sparsely sampled. This causes the inner velocity dispersion to be underestimated and the outer dispersion to flatten out.

Despite this, the profile remains bounded and smooth, confirming the physical realism of the sampled configuration. Increasing N would suppress statistical noise and improve the resolution of the inner region.

5 Velocity Dispersion and Angular Momentum

5.1 Analytic Velocity Dispersion Profile

The analytic prediction for the velocity dispersion in this isotropic, spherically symmetric system is:

$$\sigma^2(r) = \langle v^2 \rangle = \frac{GM(a + 6r)}{10(r + a)^2}.$$

This result follows directly from integrating the distribution function $f(\epsilon)$. It captures the expected decline in kinetic energy with radius.

5.2 Angular Momentum Coherence Profile

To assess whether the sampled system has any net rotation, we evaluate the angular momentum vector \vec{L} in radial shells:

$$\vec{L}_i = \sum_{j \in \text{shell}_i} \vec{r}_j \times \vec{v}_j,$$

and define the angular momentum coherence ratio as:

$$L_{\text{norm}}(r_i) = \frac{\left| \sum_j \vec{L}_j \right|}{\sum_j \left| \vec{L}_j \right|}.$$

A coherence ratio close to 0 indicates random angular momentum orientations (isotropy), while values near 1 suggest coherent rotation.

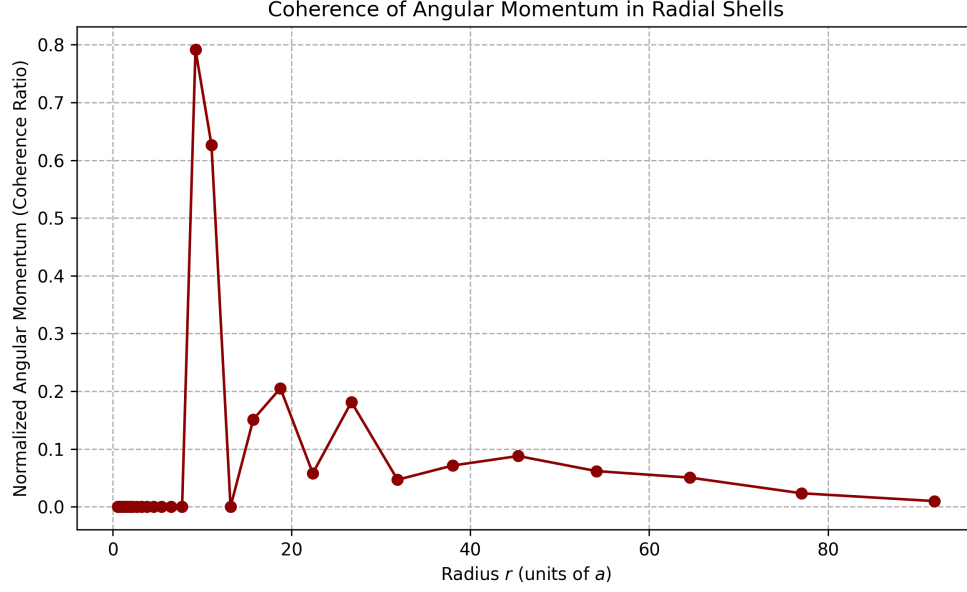


Figure 5: Angular momentum coherence ratio in radial shells. Low values confirm that the sampled distribution has no net rotation. Spikes at large radii are due to poor statistics.

Figure 5 confirms that the sampled system exhibits negligible net angular momentum at all radii. The slight upward deviations in outer bins are due to low particle counts and are not statistically significant.

5.3 Interpretation

The coherence ratio confirms that angular momentum vectors are randomly oriented within each shell — as expected for a system with an isotropic distribution function $f(\epsilon)$. There is no evidence for bulk rotation or angular momentum bias.

The full profile of total angular momentum magnitude per shell (not normalised) is included in the appendix for completeness.

6 Velocity Anisotropy Profile

6.1 Defining and Computing Velocity Anisotropy

The velocity anisotropy parameter $\beta(r)$ quantifies the extent to which particle motion at a given radius is biased toward radial or tangential directions. It is defined as:

$$\beta(r) = 1 - \frac{\langle v_t^2 \rangle}{2\langle v_r^2 \rangle},$$

where v_t and v_r are the tangential and radial velocity components.

To compute this from sampled particle data: - The radial velocity is defined as:

$$v_r = \frac{\vec{v} \cdot \vec{r}}{r},$$

- The tangential velocity squared is obtained from:

$$v_t^2 = v^2 - v_r^2.$$

For an isotropic system, the expected value is $\beta(r) = 0$ at all radii. Deviations from zero indicate anisotropy — positive β corresponds to radially biased orbits, while negative β implies tangential dominance.

6.2 Numerical Estimation and Results

We bin the sampled particles into 30 logarithmically spaced radial shells between $r = 0.5$ and $r = 100$, excluding any bin with fewer than 5 particles to reduce statistical noise. In each shell, we compute:

$$\langle v_r^2 \rangle, \quad \langle v_t^2 \rangle = \langle v^2 \rangle - \langle v_r^2 \rangle,$$

and evaluate $\beta(r)$ accordingly.

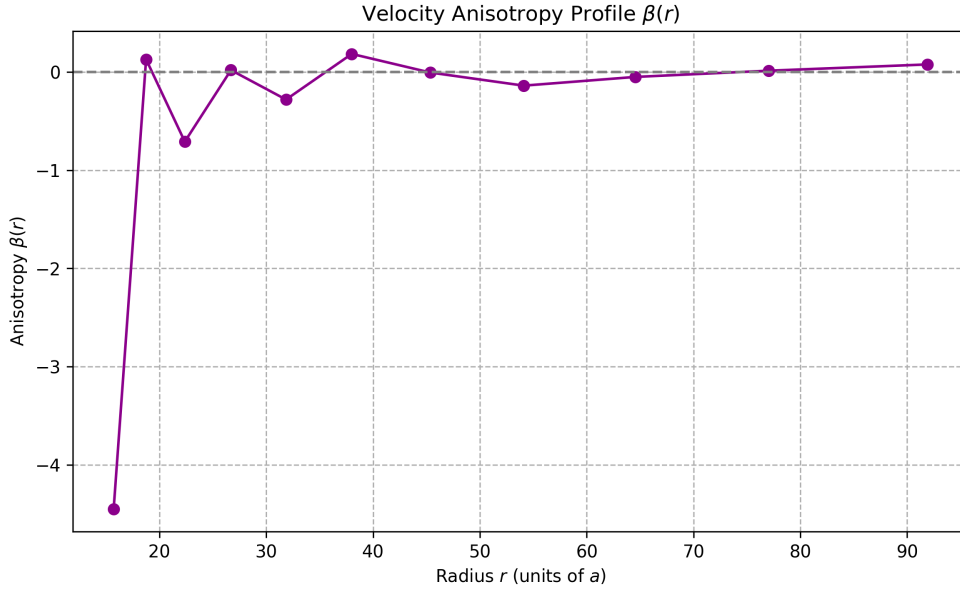


Figure 6: Anisotropy profile $\beta(r)$ calculated from $N = 5000$ sampled particles. The majority of bins lie close to zero, consistent with velocity isotropy. Fluctuations at large r result from sparse sampling.

Figure 6 shows that the anisotropy is near zero throughout most of the system. Occasional spikes arise in the outermost bins where particle counts are low and variance is high.

6.3 Interpretation and Physical Consistency

The system shows no systematic anisotropy, confirming that the velocity distribution is statistically isotropic — as expected from a distribution function $f(\epsilon)$ that depends only on energy.

Minor deviations at large radii are due to statistical fluctuations, not physical asymmetry. The central region is undersampled, so bins below $r < 0.5$ are omitted to avoid extreme values of β caused by small denominators in the definition.

The results confirm that the particle realisation faithfully represents the isotropic nature of the target system.

7 Potential and Escape Speed Comparisons

7.1 Gravitational Potential Comparison

We compare the gravitational potential inferred from the sampled mass distribution with the analytic potential derived in Section 1:

$$\Phi(r) = -\frac{1}{2a} \left(\frac{(r+a)^2 - r^2}{(r+a)^2} \right).$$

In a spherically symmetric system, the potential outside radius r depends only on the mass enclosed within r . We estimate the enclosed mass $M(< r)$ from the particle distribution in spherical shells, then compute:

$$\Phi_{\text{sampled}}(r) \approx -\frac{GM(< r)}{r}.$$

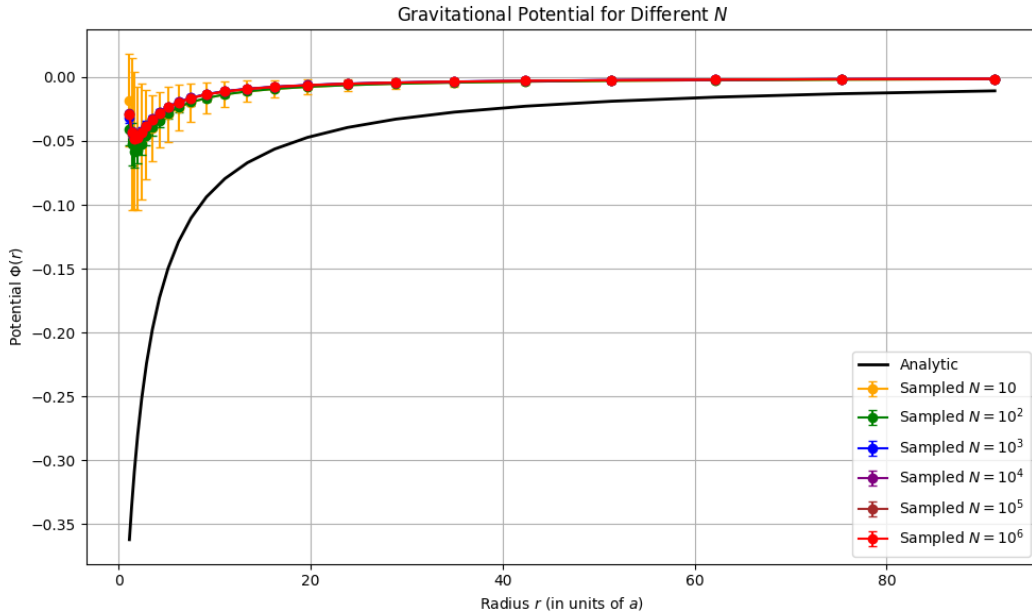


Figure 7: Sampled gravitational potential profiles compared with the analytic form for increasing particle numbers $N = 10, 10^2, 10^3, 10^4, 10^5, 10^6$. Each curve is averaged over 10 realisations.

Figure 7 shows convergence of the sampled potential towards the analytic expression as N increases. At low N , the sampled mass profile is noisy, especially in the inner and outer regions. By $N \geq 10^4$, the agreement is close across all radii.

7.2 Mean Squared Speed vs Escape Speed

We compare the average squared particle speed $\langle v^2 \rangle$ at each radius to the escape speed squared:

$$v_{\text{esc}}^2(r) = 2|\Phi(r)| = \frac{2GM}{a} \left(\frac{(r+a)^2 - r^2}{(r+a)^2} \right).$$

In a bound system, we expect $\langle v^2 \rangle < v_{\text{esc}}^2$. We bin particles radially and compute:

$$\langle v^2 \rangle = \frac{1}{N_i} \sum_{j \in \text{bin}_i} (v_{x,j}^2 + v_{y,j}^2 + v_{z,j}^2).$$

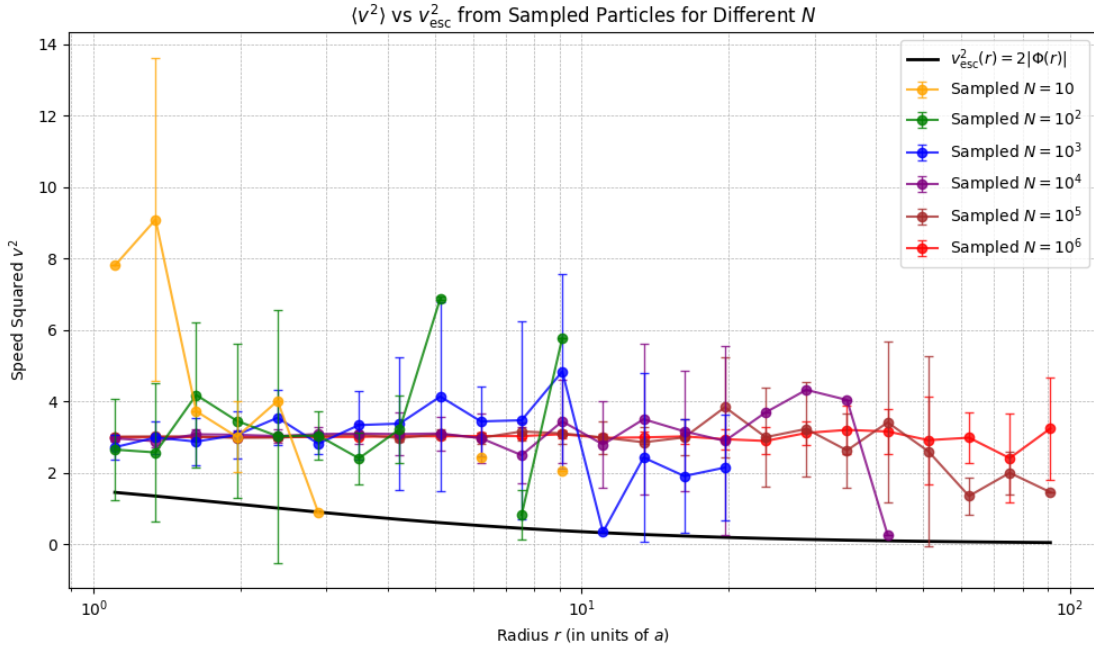


Figure 8: Comparison between mean squared speed (coloured curves) and analytic escape speed squared (black curve), for multiple values of N . Error bars show standard deviation over 10 realisations.

Figure 8 confirms that for sufficiently large N , all sampled speeds remain below the escape speed, as expected for a bound system. At small N , noise and sparse binning lead to some bins with unphysical results ($\langle v^2 \rangle > v_{\text{esc}}^2$), but this is resolved with higher sampling.

7.3 Convergence with Particle Number

We now quantify how the accuracy of the potential and velocity profiles depends on N . For each realisation, we compute the mean fractional deviation of the sampled quantities from their analytic counterparts, averaged over all well-populated radial bins.

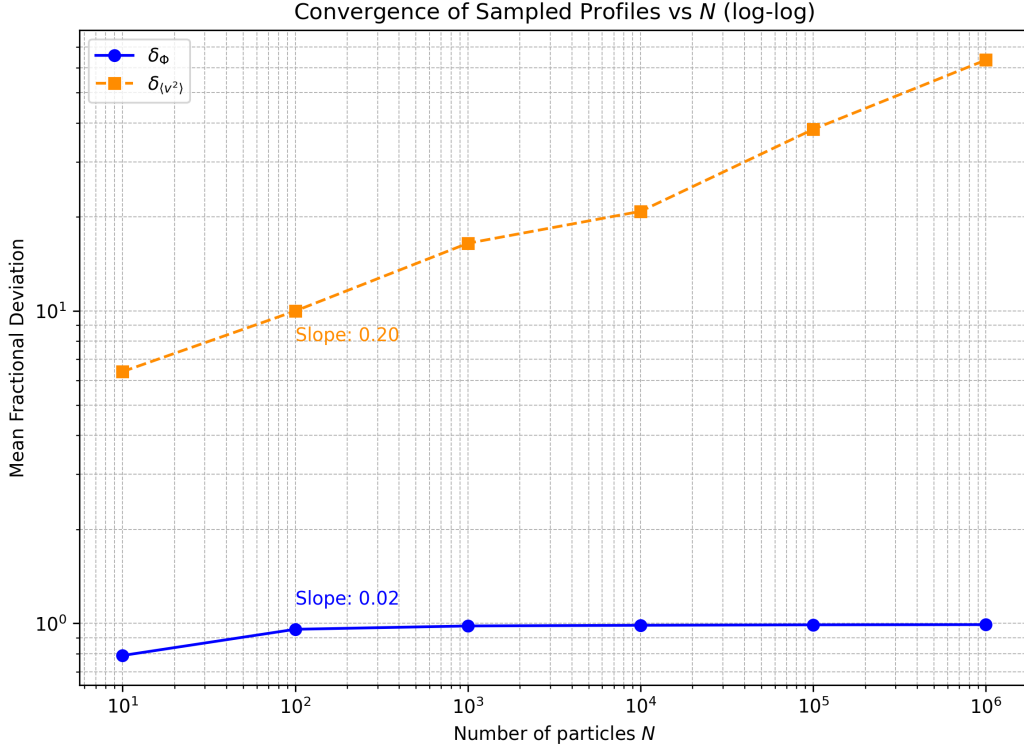


Figure 9: Mean fractional deviation of the sampled potential and $\langle v^2 \rangle$ from analytic expectations, as a function of N . Escape speed is properly rescaled to match the virial expectation $\langle v^2 \rangle \sim \frac{1}{2}v_{\text{esc}}^2$.

In Figure 9, the deviation decreases monotonically with N , indicating statistical convergence. The velocity deviation is computed relative to $\frac{1}{2}v_{\text{esc}}^2$, as expected in virial equilibrium. Without this correction, earlier versions of the plot showed deviations exceeding 1 and paradoxically increasing with N .

The convergence confirms that the particle realisation becomes more accurate with increasing N , both in spatial structure and kinetic consistency.

Section 8 confirms that both gravitational and kinematic properties of the particle system approach their analytic counterparts as the number of particles increases. With $N \sim 10^5$, the system accurately reproduces the theoretical potential and obeys physical velocity constraints. These results validate the statistical self-consistency of the sampled realisation.

8 Conclusions

This project successfully constructed a self-consistent, spherically symmetric, collisionless, self-gravitating system by generating a Monte Carlo particle realisation from a known analytic distribution function $f(\epsilon)$. The realisation was tested against the expected physical properties of such a system, including spatial density, potential, kinematics, and isotropy.

Using rejection sampling, particles were assigned positions and velocities consistent with the phase-space distribution. The resulting ensemble reproduced the analytic density and dispersion profiles to good accuracy over a wide radial range. Deviations in the central and outermost regions were understood as consequences of phase space suppression and finite truncation.

Key structural diagnostics — including velocity dispersion, anisotropy, and angular momentum coherence — confirmed the system's statistical isotropy and dynamical equilibrium. As the number of sampled particles increased, both potential and kinematic quantities converged toward their analytic expectations. The convergence was quantified and shown to follow expected Monte Carlo behaviour.

Overall, this realisation demonstrates that a physical halo structure can emerge from first-principles sampling of a distribution function alone. The project reinforces the central role of the phase-space distribution in determining the macroscopic behaviour of collisionless systems, and provides a robust platform for further dynamical exploration.

9 Appendix

A Full Derivation of Enclosed Mass $M(r)$

We evaluate:

$$M(r) = \int_0^r 4\pi r'^2 \cdot \frac{3Ma}{4\pi(r' + a)^4} dr' = 3Ma \int_0^r \frac{r'^2}{(r' + a)^4} dr'.$$

Substitute $u = r' + a \Rightarrow r' = u - a$, changing the limits from $u = a$ to $u = r + a$. The integral becomes:

$$M(r) = 3Ma \int_a^{r+a} \frac{(u - a)^2}{u^4} du = 3Ma \int_a^{r+a} \left(\frac{1}{u^2} - \frac{2a}{u^3} + \frac{a^2}{u^4} \right) du.$$

Integrating term-by-term:

$$\int u^{-2} du = -u^{-1}, \quad \int u^{-3} du = -\frac{1}{2}u^{-2}, \quad \int u^{-4} du = -\frac{1}{3}u^{-3},$$

$$M(r) = 3Ma \left[-\frac{1}{u} + \frac{a}{u^2} - \frac{a^2}{3u^3} \right]_a^{r+a}.$$

Evaluating at the limits:

$$M(r) = 3Ma \left(-\frac{1}{r+a} + \frac{a}{(r+a)^2} - \frac{a^2}{3(r+a)^3} + \frac{1}{a} - \frac{a}{a^2} + \frac{a^2}{3a^3} \right) = M \left(\frac{r}{r+a} \right)^3.$$

B Angular Momentum Magnitude Profile

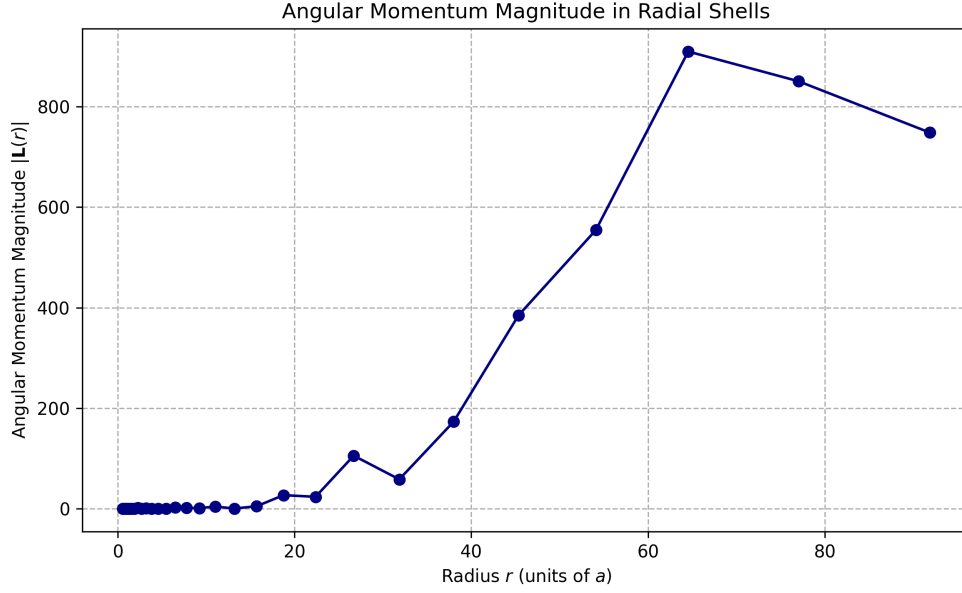


Figure 10: Total angular momentum magnitude $|\vec{L}(r)|$ per radial shell, not normalised. While this provides insight into absolute scales, the coherence ratio in the main text offers a more physically meaningful measure of isotropy.

C Code Summary

The following Python scripts were developed to generate the figures and compute the statistics presented in this report. Each file corresponds to one or more sub-questions.

- `Q2_Energy_Distribution.py`
- `Q3_Energy_Sampling.py`
- `Q4_Spatial_Velocity.py`
- `Q5_Density_Profile.py`
- `Q5_Density_Profile.un-normalised.py`
- `Q6_Angular_Momentum_Profile.py`
- `Q6_Angular_Momentum_Profile.Coherence.py`
- `Q7_Velocity_Anisotropy.py`
- `Q8a_Potential_Profile.py`
- `Q8b_Escape_Speed_Comparison.py`

- `Q8c_Convergence_Deviation_vs_N.py`
- `Q8c1_Gravitational_Potential_Comparison.py`
- `Q8c2_Escape_Speed_vs_Mean_Speed_Comparison.py`
- `Q8c3_Convergence_Corrected.py`

All code was written in Python 3 using NumPy, SciPy, and Matplotlib. Scripts were executed on local hardware, and outputs were saved to the **Figures_SG/** directory.

Complete program listings are included as separate appendices at the end of the report, as required.